Optics Letters

Reconfigurable photoinduced terahertz wave modulation using hybrid metal–silicon metasurface

AHASAN ULLAH,[1] YI-CHIEH WANG,[1] SANJIDA YEASMIN,[1] YIJING DENG,[2] JUN REN,[2] YU SHI,[2] LEI LIU,[2] AND LI-JING CHENG[1,*]

[1] *School of Electrical Engineering and Computer Science, Oregon State University, Corvallis, Oregon 97331, USA*
[2] *Department of Electrical Engineering, University of Notre Dame, Notre Dame, Indiana 46556, USA*
**Corresponding author: chengli@oregonstate.edu*

Received 16 March 2022; revised 2 May 2022; accepted 2 May 2022; posted 3 May 2022; published 20 May 2022

We present a photoinduced reconfigurable metasurface to enable high spatial resolution terahertz (THz) wave modulation. Conventional photoinduced THz wave modulation uses optically induced conductive patterns on a semiconductor substrate to create programmable passive THz devices. The technique, albeit versatile and straightforward, suffers from limited performance resulting from the severe lateral diffusion of the photogenerated carriers that undermines the spatial resolution and conductivity contrast of the photoinduced conductive patterns. The proposed metasurface overcomes the limitation using a metal-jointed silicon mesa array with subwavelength-scaled dimensions on an insulator substrate. The structure physically restrains the lateral diffusion of the photogenerated carriers while ensuring the electrical conductivity between the silicon mesas , which is essential for THz wave modulation. The metasurface creates high-definition photoconductive patterns with dimensions smaller than the diffusion length of photogenerated carriers. The metasurface provides a modulation depth of −20 to −10 dB for the THz waves between 0.2 to 1.2 THz and supports a THz bandpass filter with a tunable central frequency. The new, to the best of our knowledge, design concept will benefit the implementation of reconfigurable THz devices.

https://doi.org/10.1364/OL.457573

Manipulation of THz waves in a reconfigurable approach allows for multiple functionalities, such as THz wave switching, focusing, phase control, beam steering, filtering, and imaging, with reduced system complexity [1–5]. Various techniques have been developed to achieve tunable devices for spatial modulation of THz waves in a dynamic fashion. Many of them rely on prepatterned circuits to electrically control the wiring of the conductive patterns to support limited functionality [6–8]. An alternative way is to apply optical projections on a semiconductor substrate to produce photoconductive patterns with high flexibility. We experimentally demonstrated THz wave modulations using digital light processing (DLP) to generate programmable conductive patterns on a planar undoped silicon wafer [9]. Satisfactory modulation depths, ranging from −10 to −20 dB, with a modulation speed of the order of milliseconds, were achieved using a low-power optical projection. The technique was applied to realize polarization, beam focusing, coded-aperture imaging, and real-time THz imaging [10,11]. Despite the versatile and tunable nature of the techniques, the poor spatial resolution of the photoinduced conductive patterns significantly restricts their applications. The unsatisfactory spatial resolution results from the fact that the photogenerated carriers can diffuse hundreds of micrometers across the boundary of the optical pattern projected on the silicon substrate [12]. The severe lateral diffusion of photocarriers prohibits the method from producing any hundred-micrometer-sized photoconductive patterns with enough degree of detail. The carrier diffusion issue can be suppressed by using a semiconductor with a shorter carrier recombination lifetime τ_r, such as GaAs, which has $\tau_r \sim 10^{-8}$ s, much smaller than the 10^{-4} s in silicon [13]. However, on the downside, the small τ_r implies that a much higher optical power density, e.g., using a high-power pulsed laser, is required to excite enough carrier concentration in GaAs for THz modulation [14].

In this paper, we propose a silicon metasurface that dramatically eliminates the lateral diffusion of the photogenerated carriers to enable photoinduced THz modulation with high spatial resolution. As illustrated in Fig. 1, the photoinduced modulator uses a DLP device to project optical patterns on the metasurface using a CW light source, such as an LED. An indium tin oxide (ITO) plate, which is transparent to visible light but reflective to THz waves, is mounted at 45° with respect to the paths of both the incident THz beam and the optical illumination, serving as a beam combiner [9]. The optical projection creates programmable conductive patterns on the metasurface for THz wave modulation.

The metasurface built on an insulating substrate, e.g., glass, quartz, or sapphire, comprises an array of 10-µm- or 4-µm-thick undoped silicon mesa structures connected by discrete metal joints. The dimensions of the silicon mesas and metal joints are much smaller than the THz wavelength. A 90-nm-thick SiO_2 anti-reflection layer is coated on the silicon mesa to minimize the reflection of 550-nm optical illumination. The undoped silicon mesas stay insulating in the dark and become electrically conductive under optical illumination due to the photogeneration of excess carriers. The isolated silicon mesas physically confine the photogenerated carriers within each structure, hindering the

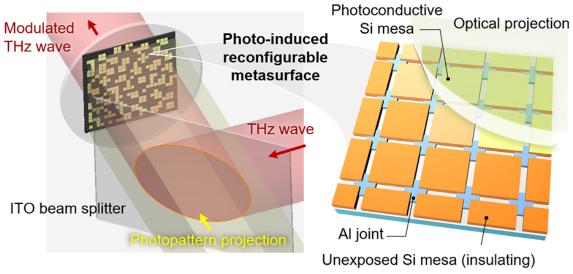

Fig. 1. Schematics of a metasurface composed of metal jointed silicon mesa array for high definition photoinduced modulation of THz waves.

lateral diffusion of photocarriers. Therefore, the optical patterns can be replicated into the photoconductive patterns on the silicon mesa array. Each silicon mesa has a size of a few to tens of micrometers allowing for creating photoconductive patterns with high spatial resolution. The discrete metal joints are arranged to connect the neighboring silicon mesas electrically. The electrical connections between the photoconductive mesas are required to form a continuous conductive pattern to block THz waves. The arrangement renders the metasurface transparent to THz waves when the silicon mesas are not optically excited. The metasurface takes advantage of silicon's large τ_r to enable photoconductivity with low-power optical excitation while constraining the lateral diffusion resulting from the large τ_r.

The conductivity of the undoped silicon mesa is determined by the photogenerated carrier concentration, regulated by the power density of optical illumination. Figures 2(a) and 2(b) summarize the carrier concentrations in the silicon mesas of different dimensions excited by 550-nm light at various power densities. The dimensions of the metasurface structures are listed in Fig. 2(c). The carrier concentrations in the silicon mesas were obtained by calculating their 3D photogeneration rates using finite-difference time-domain (FDTD) simulations (Ansys Lumerical), which were then employed to generate carrier concentration profiles. Due to its confined geometry, the resulting carrier concentrations are almost uniformly distributed in the mesa structure. Overall, the carrier concentration in the silicon mesa increases with the optical power density and slightly declines with the decrease in the mesa array period. The decreased carrier concentration can be attributed to the fact that as the silicon mesa shrinks, surface recombination becomes more influential to the carrier concentrations in the silicon mesa. Considering that the 6-μm period silicon mesa yields a photocarrier concentration comparable to the large-scaled mesas, we choose the small silicon mesa for the rest of the study to achieve high-resolution photoconductive patterns. Figure 2(d) shows that the 4-μm-thick silicon mesa holds a higher photocarrier concentration than the 10-μm-thick counterpart. With a similar carrier generation rate produced in both silicon mesas, a thinner silicon film provides less volume for the photogenerated carriers to redistribute, resulting in a higher carrier concentration at steady state. The result agrees with our previous analytical treatments on planar silicon thin films [13].

To elucidate the THz modulation property of the metasurface, we investigate the transmission spectra and modulation depths of different mesa array structures. The THz transmission spectra were obtained using FDTD simulations using the photogenerated carrier concentration shown in Fig. 2.

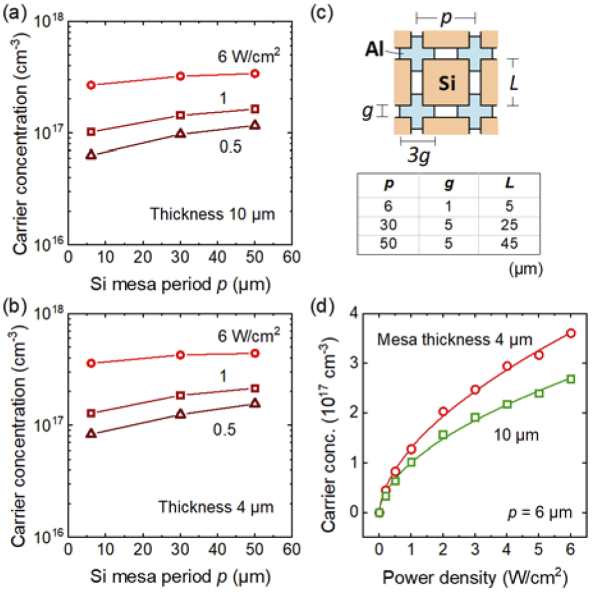

p	g	L
6	1	5
30	5	25
50	5	45

Fig. 2. Photogenerated carrier concentrations in (a) 10-μm- and (b) 4-μm-thick undoped silicon mesas with different periods ($p = 6$, 30, and 50 μm). (c) Layout and dimensions of an aluminum (Al)-jointed mesa structure with length L and gap size g for the corresponding mesa array period p. (d) Carrier concentrations in 4-μm- and 10-μm-thick silicon mesas of 6-μm period at various optical power density. The structures are all excited at 550-nm wavelength.

With the calculated carrier concentration N_e, the frequency-dependent complex dielectric permittivity functions $\epsilon(\omega) = \epsilon_{re}(\omega) + i\,\epsilon_{im}(\omega)$ of silicon in the THz spectral range can be obtained using a Drude model:

$$\epsilon_{re}(\omega) = \epsilon_\infty - \frac{\omega_{pe}^2}{\omega^2 + \gamma_e^2} - \frac{\omega_{ph}^2}{\omega^2 + \gamma_h^2}, \tag{1}$$

$$\epsilon_{im}(\omega) = \frac{\omega_{pe}^2\,\gamma_e}{\omega(\omega^2 + \gamma_e^2)} + \frac{\omega_{ph}^2\,\gamma_h}{\omega(\omega^2 + \gamma_h^2)}, \tag{2}$$

where ω is the frequency of THz radiation, $\omega_{pe,h} = \sqrt{N_e\, q^2/(m_{e,h}\epsilon_0)}$ is the plasma frequencies for electrons and holes, ϵ_∞ the dielectric constant of silicon, ϵ_0 the permittivity of vacuum, and m_e and m_h the effective masses of electron and hole, respectively. The electron and hole damping coefficients, γ_e and γ_h, are calculated by the inverse of the average electron or hole collision time depending on the effective mass $m_{e,h}$ and the mobility $\mu_{e,h}$ of carriers, i.e., $\gamma_{e,h} = (m_{e,h}\,\mu_{e,h}/q)^{-1}$ [13]. Note that the dielectric permittivity functions vary with optical excitation power density.

Figure 3 summarizes the THz transmission properties of different structures on a 50-μm glass substrate. The transmission spectrum in Fig. 3(a) shows that the 2-μm-thick Al mesh efficiently blocks THz waves, especially at the low-frequency range. Decreasing the mesh period from 50 μm to 6 μm drastically reduces the THz transmission. However, a discrete Al joint array in Fig. 3(b), which is essentially the broken Al mesh, is highly transmissive to THz waves. The transmissions are greater than 85% regardless of the array period. Because the

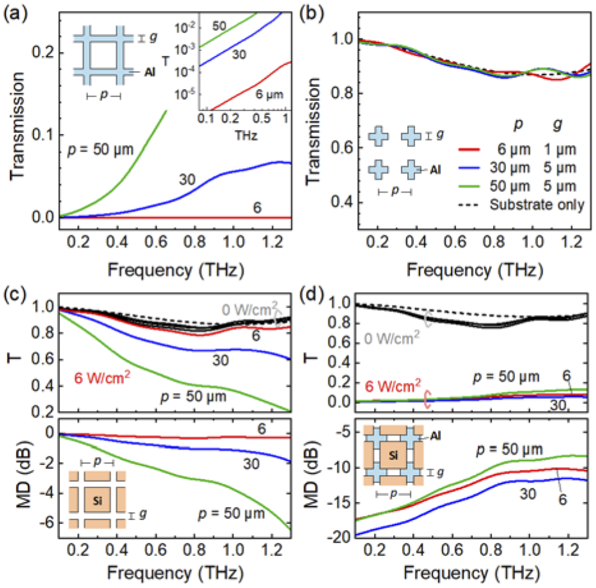

Fig. 3. Transmission spectra of (a) Al mesh and (b) discrete Al joint array. Transmission (T) spectra and modulation depth (MD) of (c) isolated silicon mesa array, and (d) hybrid mesa array under 0- and 6-W/cm^2 optical illuminations. The Al joints are 2 μm thick, and the silicon mesas are 4 μm thick. The value *p* indicates the period of the structures, and the corresponding *g* is the width of the Al mesh (joints) or the gap size of the mesa array. The dashed traces in panels (b), (c), and (d) represent the transmission spectra of the glass substrate without any structure.

Al joints are much smaller than the THz wavelength of interest, their transmission spectra basically follow the response of the glass substrate, indicated by the dashed trace. Figure 3 (c) shows that the isolated silicon mesa arrays without optical illumination are also permeable to THz waves with transmissions larger than 80% disregarding the mesa array period. Under 6-W/cm^2 optical excitation, the 50-μm period silicon mesa array slightly blocks the THz waves at higher frequencies, yielding a modulation depth of approximately −5 dB, not enough for THz wave modulation. The 6-μm period silicon mesa array does not provide any modulation capability even though the silicon mesas are conductive under photoexcitation. The THz responses in Figs. 3(b) and 3(c) suggest that the conductive patterns with sub-THz wavelength dimension will not impact the transmission of THz waves. Combining the isolated silicon mesa array and the discrete Al joints forms a hybrid mesa array, as shown in Fig. 3(d). The silicon mesa serves as a light-controlled electrical gate that regulates the electrical connectivity of the mesh network—the hybrid mesa array functions as a reconfigurable metasurface. Without optical excitation, the hybrid mesa array is essentially composed of the discrete metal joint array connected by insulating silicon mesas and is transmissive to THz waves. An optical pattern projected onto the hybrid mesa array controls the electrical connectivity of the array and produces continuous conductive patterns for THz wave modulation. Figure 3(d) shows that illuminating 6-W/cm^2 light on the hybrid mesa array significantly cut off the THz transmission, leading to a modulation depth ranging from −10 to −20 dB. The result is close to the −15- to −20-dB modulation depth obtained using an undoped silicon thin film of the same thickness.

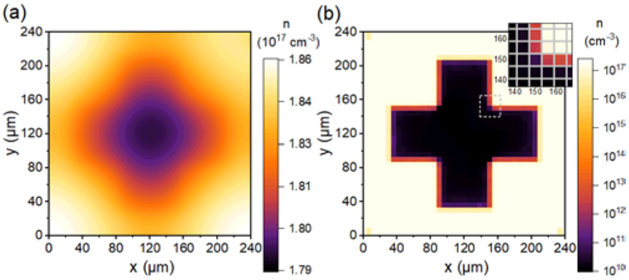

Fig. 4. Carrier concentration profiles on (a) a 4-μm-thick undoped silicon thin film and (b) a metal-jointed silicon mesa array with 4-μm-thick silicon mesa and 6-μm period illuminated by a 6-W/cm^2 optical pattern with a 180-μm-wide hollow cross symbol. The inset in panel (b) indicates the concentration profile of the hybrid mesa array in the area enclosed by the dashed box. Note that the carrier concentrations are plotted in linear scale for panel (a) and log scale for panel (b).

Efficient THz modulation aside, the hybrid mesa array allows for precisely converting the projected light patterns into photoconductive patterns. We investigated the light-induced photoconductive patterns using Lumerical FDTD and Charge solvers. Figures 4(a) and 4(b) compare the resulting photogenerated carrier concentration profiles on an undoped silicon thin film and a metasurface exposed to an optical pattern with a 180-μm-wide hollow cross. The region except the cross-shape pattern is under 6-W/cm^2, 550-nm light exposure. Since the optical pattern has a dimension comparable to the carrier diffusion length in silicon, it is not possible to transfer the optical pattern into the corresponding carrier concentration distribution on the silicon thin film with an acceptable resolution. Figure 4(a) shows that the diffusion of the photogenerated carriers severely smudges the hollow cross pattern on the silicon thin film. The permittivity function is almost identical throughout the silicon thin film with poor contrast in carrier concentration (<4%). The issue also happens to large photoinduced patterns (Fig. S1 in Supplement 1). The lateral carrier diffusion tends to be more severe in a thin film than bulk silicon due to the restricted diffusion in the vertical direction [13].

The hybrid mesa array in Fig. 4(b), in contrast, yields a high-resolution carrier concentration profile that accurately duplicates the hollow cross pattern from the optical illumination. The silicon mesa array physically confines the photogenerated carriers and successfully inhibits their lateral diffusion. The metal joints connecting between silicon mesas ensure electrical conductivity and simultaneously block the out-diffusion of the excess carriers from each silicon mesa. The boundary of the cross pattern on which the silicon mesas are partially illuminated contains an intermediate carrier concentration level, which can be observed in the inset of Fig. 4(b). The carrier concentrations in the illuminated and unexposed regions can defer by seven orders, leading to an insulating cross pattern surrounded by a conductive surface that resembles a cross-shape aperture formed on a metallic thin film.

The photoinduced conductive patterns are pixelated with the spatial resolution determined by the mesa array period, which can be further scaled based on the applications. The minimum spatial resolution may be restricted by the fabrication capability and the diffraction limit of light projection. The investigation also indicates that the unexposed region on the hybrid mesa

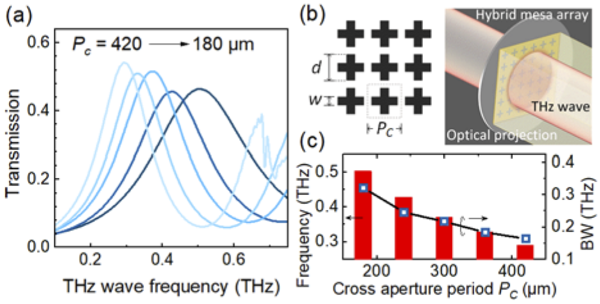

Fig. 5. (a) Transmission spectra, (b) illustration, and (c) central frequency and bandwidth (BW) of the photoinduced cross aperture filters with various dimensions produced on the metal-jointed silicon mesa array with 4-μm-thick silicon mesa and 6-μm period. The period P_c, length d, and width w of the photoinduced cross aperture array are summarized in Table 1.

Table 1. Dimensions of the Photoinduced Cross Aperture Array

Period P_c (μm)	180	240	300	360	420
Width w (μm)	48	60	78	90	105
Length d (μm)	138	225	228	270	318
Frequency (THz)	0.503	0.428	0.371	0.329	0.291

array can experience a small amount of light scattered from the nearby illuminated mesa structures. The light leakage does not create a noticeable generation rate in the unexposed area with a dimension larger than a few tens of micrometers. However, the issue may impact the contrast of the photoconductive patterns as the optical pattern scales down but could be resolved by using a collimated optical projection.

The programmable feature of the hybrid mesa array allows unlimited types of photoconductive patterns. Here we demonstrate a reconfigurable THz bandpass filter capable of producing tunable central frequencies. Conventional bandpass filters can be realized using an array of cross-shaped apertures fabricated on a metal film [15]. The period and dimension of the cross aperture array determine its central frequency. With the high-definition photoinduced cross aperture pattern on the hybrid mesa array demonstrated in Fig. 4(b), it is possible to create a two-dimensional array of such patterns with adjustable dimensions to achieve a tunable bandpass filter. The photogenerated carrier concentrations obtained in Fig. 4(b) were employed to construct bandpass filters. Figure 5(a) shows the transmission spectra of five different photoinduced cross aperture array filters with the dimension summarized in Table 1. When the period of the photoinduced cross aperture array increases from 180 to 420 μm, the central frequency shifts from 0.503 to 0.291 THz, and the bandwidth decreases from 0.322 to 0.164 THz. It is worth noting that the metal joints are required in connection with the silicon mesa array to enable continuous conductive patterns for efficient THz wave modulation. The isolated silicon mesa array cannot provide the demonstrated filter function (Fig. S2 in Supplement 1) because an array of sub-THz wavelength structured mesas remain transparent to THz waves even they are conductive under optical excitation [16].

To conclude, we demonstrated a new concept for high-resolution programmable THz wave modulation using a metasurface based on a metal jointed silicon mesa array. The subwavelength-scaled metal joints and silicon mesas without optical illumination are transparent to THz waves. The large carrier recombination lifetime of silicon supports photoconductivity under low-power optical excitation. The confined geometry of the isolated mesa structures terminates the lateral diffusion of photogenerated carriers, enabling high-resolution high-contrast photoconductive patterns. The subwavelength metal connections between the silicon mesas also efficiently stop the carrier diffusion and, more importantly, provide the required electrical connections between the photoconductive silicon mesas to allow efficient modulation of THz waves. Increasing the photogenerated carrier concentration in the excited metasurface will further improve the THz modulation depth and was also found to boost the quality factor of the tunable bandpass filter, which will be reported in the future. The improvement can be achieved by replacing silicon with other materials with a larger carrier recombination lifetime or eliminating surface recombination. Overall, the proposed metasurface is expected to enhance the spatial resolution of coded aperture imaging and realize multifunctional THz devices, such as beam focusing and steering, that cannot be achieved in traditional approaches.

Funding. National Science Foundation (ECCS-1711052, ECCS-1711355).

Disclosures. The authors declare no conflicts of interest.

Data availability. Data underlying the results presented in this paper are not publicly available at this time but may be obtained from the authors upon reasonable request.

Supplemental document. See Supplement 1 for supporting content.

REFERENCES

1. H.-T. Chen, J. F. O'Hara, A. K. Azad, A. J. Taylor, R. D. Averitt, D. B. Shrekenhamer, and W. J. Padilla, Nat. Photonics **2**, 295 (2008).
2. Y. Monnai, K. Altmann, C. Jansen, H. Hillmer, M. Koch, and H. Shinoda, Opt. Express **21**, 2347 (2013).
3. A. Kannegulla, Z. Jiang, S. M. Rahman, M. I. B. Shams, P. Fay, H. G. Xing, L.-J. Cheng, and L. Liu, IEEE Trans. Terahertz Sci. Technol. **4**, 321 (2014).
4. L. Gingras, A. Jaber, A. Maleki, O. Reshef, K. Dolgaleva, K. Dolgaleva, R. W. Boyd, R. W. Boyd, R. W. Boyd, and J.-M. Ménard, Opt. Express **28**, 20296 (2020).
5. L. Gingras, W. Cui, A. W. Schiff-Kearn, J.-M. Ménard, and D. G. Cooke, Opt. Express **26**, 13876 (2018).
6. T. Kleine-Ostmann, P. Dawson, K. Pierz, G. Hein, and M. Koch, Appl. Phys. Lett. **84**, 3555 (2004).
7. X. He, T. Li, L. Wang, J. Wang, J. Jiang, G. Yang, F. Meng, and Q. Wu, J. Appl. Phys. **115**, 17B903 (2014).
8. G. Zhou, P. Dai, J. Wu, B. Jin, Q. Wen, G. Zhu, Z. Shen, C. Zhang, L. Kang, W. Xu, J. Chen, and P. Wu, Opt. Express **25**, 17322 (2017).
9. L.-J. Cheng and L. Liu, Opt. Express **21**, 28657 (2013).
10. M. I. B. Shams, Z. Jiang, S. Rahman, J. Qayyum, L.-J. Cheng, H. G. Xing, P. Fay, and L. Liu, Electron. Lett. **50**, 801 (2014).
11. L. Liu, R. Pathak, L.-J. Cheng, and T. Wang, Sens. Actuators, B **184**, 228 (2013).
12. Y. He, Y. Wang, M. Li, Q. Yang, Z. Chen, J. Zhang, J. Zhang, Q. Wen, and Q. Wen, Opt. Express **29**, 8914 (2021).
13. A. Kannegulla, M. I. B. Shams, L. Liu, and L.-J. Cheng, Opt. Express **23**, 32098 (2015).
14. G. Georgiou, H. K. Tyagi, P. Mulder, G. J. Bauhuis, J. J. Schermer, and J. G. Rivas, Sci. Rep. **4**, 3584 (2015).
15. D. W. Porterfield, J. L. Hesler, R. Densing, E. R. Mueller, T. W. Crowe, and R. M. Weikle, Appl. Opt. **33**, 6046 (1994).
16. Z. Wang, J. Qiao, S. Zhao, S. Wang, C. He, X. Tao, and S. Wang, InfoMat **3**, 1110 (2021).